THE JOURNAL OF PHYSICAL CHEMISTRY C

Article

Cite This: J. Phys. Chem. C 2019, 123, 5790−5803

pubs.acs.org/JPCC

Water Dynamics in Nanoporous Silica: Ultrafast Vibrational Spectroscopy and Molecular Dynamics Simulations

Steven A. Yamada,[†] Jae Yoon Shin,[†] Ward H. Thompson,*[,‡] and Michael D. Fayer*[,†]

[†]Department of Chemistry Stanford University, Stanford, California 94305, United States

[‡]Department of Chemistry University of Kansas, Lawrence, Kansas 66045, United States

Supporting Information

ABSTRACT: Nanoporous silica materials are important in catalysis, energy, and materials applications in which water is an essential component. System performance is intimately connected to the water dynamics occurring in the confined environment. However, the dynamics and associated structures of water in nanoporous silica have proven challenging to measure and predict. Here, confined water dynamics are examined via the ultrafast infrared spectroscopy of selenocyanate ($SeCN^-$) dissolved in the hydrated ~2.4 nm silica mesopores of MCM41. Polarization selective pump−probe and two-dimensional infrared measurements on the CN stretching mode of $SeCN^-$ are used to probe the effect of confinement on orientational relaxation and spectral diffusion dynamics. The dynamics of $SeCN^-$ provide information on the surrounding water hydrogen bond dynamics. The long CN stretch lifetime (~36 ps), relative to the water hydroxyl stretch (<2 ps), significantly extends the time scales that can be accessed. Complete orientational relaxation ($C_2(t)$, orientational correlation function) and spectral diffusion ($C_\omega(t)$, frequency−frequency correlation function) dynamics are presented and compared to the simulated time correlation functions in a model silica pore of the same size. A slow decay component not present in the bulk liquid is observed in both experiments, indicating that the hydrogen bond dynamics are significantly altered by confinement. The simulations reveal a qualitative difference in the functional dependence of $C_2(t;d)$ and $C_\omega(t;d)$ on d, the distance from the interface. The former becomes exponentially faster with distance while the latter makes an abrupt transition from slower to faster dynamics midway between the surface and pore center, $d \cong 6$ Å.

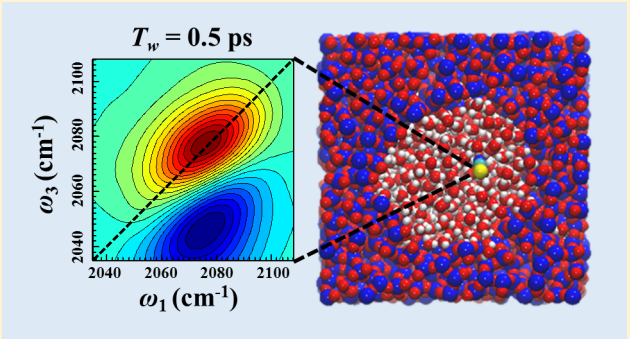

I. INTRODUCTION

Confined water plays an integral role in the structure and function of an enormous range of nanoscale systems. One notable class of systems is mesoporous silica,[1−11] of which the powder MCM41 is a prominent example. These materials are widely used as a solid support for catalytic groups in heterogeneous reactions, in which water often acts as a key reactant or solvent.[12] In addition to providing a high density of active sites by virtue of a large surface area to volume ratio, the surface of the nanoscale silica pores has a dramatic impact on the behavior of the water. For example, confinement of water in MCM41 has enabled scientists to explore the dynamics of deeply supercooled water below its homogeneous nucleation temperature,[3,13] providing the first evidence of a fragile-to-strong dynamic crossover hypothesized to exist in bulk water.

The structure of an MCM41 particle (Figure 1A) consists of uniform cylindrical pores (variable from 1.5 to 10 nm) that pack into a hexagonal 2D array along a particular direction. In the orthogonal direction, the pores extend in a parallel fashion over the length of the particle (micrometers). The pore surface features siloxane (Si−O−Si) bridges and terminal silanol (Si−OH) groups in diverse microenvironments (Figure 1A,B).[14−17] Silanols exist in isolation (i.e., non-hydrogen bonding) and engage in hydrogen bond (H-bond) interactions with nearby siloxane oxygens, other silanols, or water molecules confined in the pores. Quantifying the changes in the structure and ultrafast dynamics of water upon confinement in MCM41 is central to understanding the molecular scale details that give rise to this system's interesting and unusual properties.

Despite several theoretical predictions[6−10] and experimental insights[1−5] into water dynamics in porous silica, relatively few experimental studies have used ultrafast time-domain methods,[1,5,18,19] and of these, none have focused on the highly uniform pores present in MCM41. Ultrafast mid-IR polarization selective pump−probe (PSPP) and two-dimensional infrared (2D IR) spectroscopies are particularly useful methods for the study of water H-bond dynamics in confined systems. These methods monitor fluctuations in hydrogen bond network configurations through variations in the orientation and frequency of a vibrational mode.[5,20−22] Although water is the molecule of interest, direct study of the hydroxyl stretch of

Received: January 20, 2019
Published: January 30, 2019

DOI: 10.1021/acs.jpcc.9b00593
J. Phys. Chem. C 2019, 123, 5790−5803

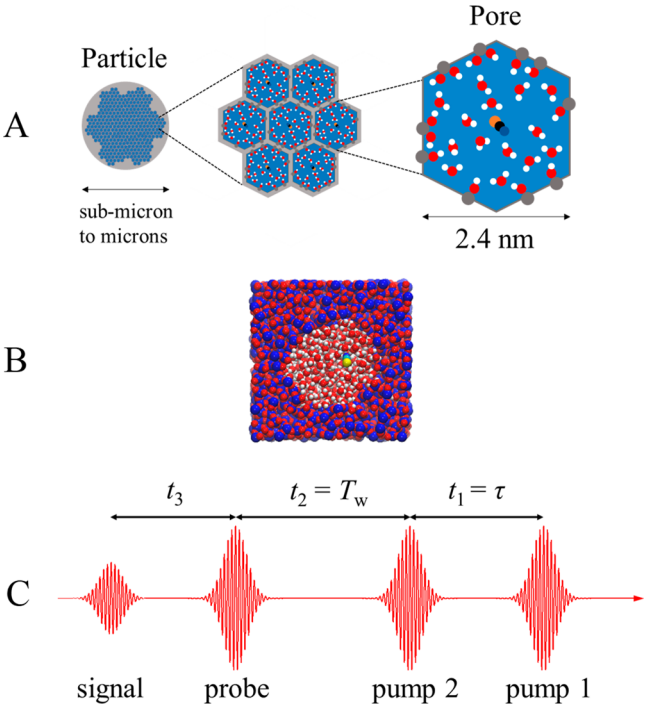

Figure 1. (A) Transverse illustration of an MCM41 particle with expanded views of the internal water filled pores (not optimized) containing the $SeCN^-$ vibrational probe used in the experiments. In contrast to a nondefective silica surface composed of hydrophobic siloxane groups,[14] the surface of MCM41 is inhomogeneous, with hydrophobic siloxane patches (depicted as empty pore surface regions) interspersed with hydrophilic silanol-rich regions. The tetrahedral (SiO_4) arrangement of atoms permits two hydrophilic surface species, single and geminal silanols, in which Si is coordinated to one or two hydroxyls, respectively.[14−17] Atoms are depicted as spheres: gray (Si), red (O), white (H), orange (Se), black (C), blue (N). (B) The model silica pore system used in the simulations. (C) General 2D IR pulse sequence with time delays between pulses defined. Time increases in the direction opposite the red arrow.

water in MCM41 with PSPP and 2D IR experiments poses several experimental issues. One unavoidable problem is the short vibrational lifetime (<2 ps) of the water hydroxyl stretching mode.[21] The resulting low signal-to-noise ratio at long time delays limits the observation of slower dynamics which are often the main signature of the confinement. Other disadvantages include pronounced heating artifacts[23] and oscillator strength that is distributed over a broad spectral range, reducing contrast between the signal and scattered electric fields from the silica particles.[24] Separation of the signals originating from the overlapping water and silanol hydroxyl absorptions is another nontrivial issue.[10] These challenges are responsible for incomplete experimental information on reorientation[5] and nonexistent 2D IR spectral diffusion measurements on water confined in the silica pores. Spectral diffusion (the time evolution of the frequency of a vibrational mode) in water proceeds through fluctuations in the number and strength of H-bonds surrounding the oscillator, making it an important observable for understanding the dynamics of confined water.[10]

The present work combines PSPP and 2D IR measurements with molecular dynamics (MD) simulations to analyze time and space-resolved dynamics in water confined in MCM41 with ∼2.4 nm diameter pores. The selenocyanate anion ($SeCN^-$) was selected as a probe of the surrounding water dynamics because it avoids many of the issues associated with studying the hydroxyl stretch of water directly, yet its spectral diffusion has been demonstrated to closely track the time scales of water in the bulk liquid.[22] An empirical frequency map has been developed for $SeCN^-$ in water,[22] providing a route to calculate its spectral diffusion in confined water. The long CN stretch vibrational lifetime (∼36 ps) permitted the observation of complete orientational relaxation and spectral diffusion in the aqueous phase of MCM41 for the first time, although not without the need for several experimental improvements. Powdered solids are challenging to study with PSPP and 2D IR experiments, as these techniques are susceptible to scattered light from the pulses that generate the signal.[24,25] The scattered light was reduced in this study using a combination of methods, ranging from the sample preparation procedure to a newly developed phase cycling scheme. In the 2D IR experiments, a previously reported method of combining mid-IR frequency-domain pulse shaping techniques[26,27] and a polarization filter[25] was successfully employed to reveal water−anion hydrogen bond dynamics in the MCM41 pores. A new phase cycling procedure was developed for the PSPP experiment, which improved the quality of data acquired in the scatter prone "parallel" polarization configuration. The strong transition dipole of the CN stretch of $SeCN^-$ also facilitated the discrimination of the desired third-order signals from scatter.

II. EXPERIMENTAL PROCEDURES

II.A. Particle Size Reduction. MCM41 was purchased from Sigma-Aldrich. The as-received powder generated considerable scattered light in the optical experiments. Because the experiments were performed in transmission mode, forward scattering of the excitation pulses into the signal detection direction (probe pulse direction, see below)[27,28] posed an issue. The first strategy used to combat scatter was to reduce the average particle size of the MCM41 sample. It is well-known that when the wavelength and particle are comparable in size, the amplitude of scattering increases with the size of the scattering particle.[29] A sedimentation procedure, outlined in the Supporting Information, was used to select smaller particles from the as-received powder. Briefly, MCM41 was placed on top of a column of water. Following 10 min, the top fraction, ∼8 in. or 20 cm of water, was vacuum filtered, and the particles were collected for later use. The duration and length of the column in principle selected particles with diameters less than ∼40 μm. The entire procedure was repeated multiple times to compensate for the low yield of smaller particles.

II.B. Surface Area, Pore Size Distribution, and Pore Volume of MCM41. The as-received and smaller particle (see section II.A) MCM41 samples were characterized with N_2(g) adsorption and desorption isotherms (Figure S1A) acquired at the Soft & Hybrid Materials Facility (SMF) at the Stanford Nano Shared Facilities (SNSF). The area of the mesoporesurface was assessed by generating BET plots[30] (Figure S1B) from the adsorption curves in Figure S1A. The mean specific BET surface area, S_{BET}, was found to be 960 ± 30 m^2/g from four independently prepared samples. The pore diameter distributions for each sample (Figure S1C) were obtained from BJH analysis[31] of the sorption isotherm curves in Figure S1A and are displayed in Figure S1C. Analysis of the adsorption or desorption curves gave identical results. The narrow

DOI: 10.1021/acs.jpcc.9b00593
J. Phys. Chem. C 2019, 123, 5790−5803

distributions (fwhm ~ 5 Å) were virtually identical, giving an average pore diameter of 2.5 ± 0.2 nm. Thus, the MCM41 pore diameter is identical, within error, to the diameter of the silica pore model used in the simulations (2.4 nm). The homogeneity of the material was further confirmed in the experiments, with high reproducibility observed for both the rotational and spectral diffusion measurements made on several samples. The primary mesopore volume[32,33] was also determined to be 0.8 ± 0.1 cm^3/g. Further details on the methods and calculations are provided in the Supporting Information.

II.C. Sample Hydration. Details of the sample hydration are provided in the Supporting Information. Solutions and powders described in this section were prepared and manipulated under an N_2(g) atmosphere. Briefly, completely dry MCM41 powder (of smaller particle size) was gently mixed in 0.3 M KSeCN/D_2O solution. The particles were filtered to remove bulk solution from the sample. Variable degrees of hydration were obtained sample-to-sample following the filtration step, and it was found that the measured dynamics were very sensitive to the amount of solution in the sample. To obtain reproducible dynamics, each sample was equilibrated overnight in a home-built hydration chamber (Figure S2). The D_2O vapor pressure in the hydration chamber was maintained at 78% or 100% RH by continuously bubbling N_2(g) through a saturated NaCl/D_2O[34] or pure D_2O reservoir and flowing the vapor over the powder. The % RH was chosen to lie beyond the capillary condensation region in the room-temperature water sorption isotherm of MCM41 ($P/P_0 \sim 0.6$)[35,36] to fully hydrate the uniform primary mesopores (D = 2.5 ± 0.2 nm) in the sample. The water sorption isotherm has noticeable hysteresis between the adsorption and desorption curves.[35] We note that if the equilibration vapor pressure is too close to the hysteresis loop, markedly different hydration states can be obtained depending on the initial hydration status of the sample. The simulated dynamics were compared to the samples hydrated at 100% RH. The 78% RH data are tabulated in the Supporting Information.

II.D. Sample Cell Preparation and Linear-IR Spectroscopy. The sample cell preparation used in the linear and nonlinear-IR experiments is detailed in the Supporting Information and briefly described here. The sample cell is similar to one described previously.[22] The path length was set to 25 μm with two concentric polytetrafluoroethylene (PTFE) spacers with outer diameters of 25.4 and 13 mm, respectively. The inner diameter of the smaller spacer was ~8 mm. The MCM41 powder, prepared according to section II.C, and an index matching fluid (paraffin oil) were placed in the center of the smaller spacer. The region between the inner and outer spacers was also filled with paraffin oil. The spacers were sandwiched between two CaF_2 windows with 25.4 mm diameters and 3 mm widths. Fourier transform IR (FT IR) spectra of the KSeCN/D_2O containing MCM41 were measured with a Thermo Scientific Nicolet 6700 FT IR spectrometer purged with air scrubbed free of CO_2 and H_2O. The absorption spectrum of the silica powder containing solely D_2O with identical spacer thicknesses was measured and subtracted from the resonant sample spectrum.

II.E. 2D IR Spectroscopy. The 2D IR spectrometer used in this work has been described in detail in past publications.[22,28] The spectrometer is configured in a pump−probe geometry[27,28,37] and features a mid-IR pulse shaping system in the excitation beam path (see Figure S3A).[26−28] 2D IR and PSPP spectroscopies are resonant, third-order time-domain experiments.[37,38] In 2D IR, three pulsed electric fields interact with a material through its third-order susceptibility. Following three interactions, the induced polarization in the material emits a fourth field known as the vibrational echo signal. In the pump−probe geometry, phase matching dictates that the signal is emitted collinearly with pulse 3, the probe pulse. In addition to stimulating the echo emission, pulse 3 also serves as the local oscillator for heterodyne detection of the echo signal. In the limit of very short pulses (semi-impulsive limit),[37] the polarization is proportional to the response function of the molecular system. The response function is dependent on the dynamics of the ensemble. Time-resolved dynamics are obtained from the data in the form of two-point time correlation functions (TCFs).[38−40]

The pulse sequence is shown in Figure 1C. The measured third-order response functions are 3D functions of the time delays, $t_1 = \tau$, $t_2 = T_w$, and t_3. A more straightforward manner to visualize and analyze the response functions is to perform a 2D Fourier transform on the t_1 and t_3 axes to generate a 2D IR spectrum, $\tilde{S}(\omega_1,T_w,\omega_3)$. A 2D IR spectrum is a correlation plot with ω_3 (final frequencies) on the vertical axis and ω_1 (initial frequencies) on the horizontal axis for a fixed value of the population period (T_w). During the T_w period, the structure of the sample, and therefore the frequency of the probe, evolves. The 2D IR spectra were acquired for a series of T_w. The 2D band shape evolves from elongated along the diagonal (the line $\omega_3 = \omega_1$) to round as the correlation between initial and final frequencies decays with increasing T_w. Scatter-free 2D IR spectra were obtained in the $\langle XXYY \rangle$ polarization configuration with a four-shot scatter removal phase cycle.[25,27] In this "perpendicular" configuration, the two pump pulses were linearly polarized vertically (Y) and the third pulse and echo detection were polarized horizontally (X).

Qualitatively, 2D IR works as follows. There are four pulses in the pulse sequence (Figure 1C). Three input pulses generate the nonlinear polarization, which gives rise to the emission of a fourth pulse, the vibrational echo. The first two pulses label and store the initial frequencies, which form the horizontal axis of the 2D spectrum, ω_1. During the time between the second and third pulses, T_w, the water structure evolves. As the water structure evolves, the intermolecular interactions between water molecules and the vibrational probes change. This change in local and mesoscopic distance scale interactions changes the frequencies of the vibrational probes. The third pulse and echo read out the final frequencies, which form the vertical axis, ω_3. As T_w increases, the water structure interacting with the probes has more time to evolve, leading to more frequency change and therefore more change in the 2D IR line shape. The T_w dependence of the 2D line shape is analyzed to extract the time dependence of the water structure.

II.F. Polarization Selective Pump−Probe Spectroscopy with Scatter Reduction. PSPP spectroscopy can be regarded as a special case of 2D IR spectroscopy where the time delay, t_1, separating the first two pulses is fixed to zero (see Figure 1C). The first two sample-field interactions occur simultaneously with the arrival of a single pump pulse.[41] The third interaction occurs when the probe pulse arrives an interval, t ($t_2 = T_w$ in the echo experiment, Figure 1C), later. The PSPP signal is the transient difference in the probe intensity with the pump pulse on versus off.[41] To acquire the signal, the pump is chopped at 500 Hz, or half the laser repetition rate, with an acousto-optic modulator (AOM). The

DOI: 10.1021/acs.jpcc.9b00593
J. Phys. Chem. C 2019, 123, 5790−5803

signal is measured in two polarization configurations termed "parallel" and "perpendicular". The probe is linearly polarized at 0° (in the plane of the optical table), and the pump is linearly polarized at 45° relative to the probe. After the sample, a polarizer in a computer-controlled rotation mount resolves the signal at +45° or −45°, which correspond to parallel, $S_{\parallel}(t)$, and perpendicular, $S_{\perp}(t)$, configurations, respectively.

In the measurement of a scattering sample, the total integrated intensity on the array detector,[25] for laser shots where the pump is on, can be written

$$S_{on} \propto |E_{pr} + E_s + sE_p|^2 = S_{off} + |sE_p|^2 + E_{pr}E_s^* + s^*E_{pr}E_p^* + s^*E_sE_p^* + (\text{c. c.}) \quad (1)$$

where E_{pr}, E_s, and sE_p refer to probe, signal, and scattered pump fields (s is a complex scatter coefficient), respectively, $S_{off} = |E_{pr}|^2$, and the small homodyne signal, $|E_s|^2$, has been neglected. The explicit time dependence of the terms has been omitted. The signal of interest is the third term on the second line of eq 1. As discussed in the Supporting Information, the homodyne scatter term $|sE_p|^2$ is independent of t and can be straightforwardly accounted for by measuring the offset in the data at negative t delays (probe arriving before pump). The heterodyne scatter terms (final two terms on the second line of eq 1) not only vary in amplitude but also oscillate at the optical frequency as t is scanned (Figure S3B). To remove the heterodyne scatter, a four-shot scatter removal phase cycle (eq S7) was used to acquire the data. In addition to this, for each delay t, the delay was scanned over 200 fs, i.e., $t - \epsilon \rightarrow t + \epsilon$ (ϵ = 100 fs), using the pulse shaper. As this scanning range is comparable to the pulse duration, the pump−probe signal level is essentially invariant, while the heterodyned scatter exhibits an oscillation at the optical frequency (Figure S3B), with the desired pump−probe signal representing the average of the oscillatory signal. Thus, the pump−probe signal of interest and the heterodyned scatter can be clearly distinguished in this procedure. The acquired data were averaged over six optical periods to remove residual scatter fringes present following phase cycling.

III. SIMULATION DETAILS

III.A. System Modeling. The dynamics of $SeCN^-$ in D_2O confined in nanoscale silica pores were investigated using MD simulations based on a combination of previously developed models. In particular, the fixed-charge force field for $SeCN^-$ previously obtained from a combination of electronic structure calculations and comparisons to experiments in bulk D_2O was used.[22] The parameters, developed using the SPC/E water model[42] for D_2O, are given in Table 1 of ref 22. In brief, the key elements of the model are a symmetric charge distribution ($q_{Se} = q_N = -0.55$; $q_C = 0.1$) and a larger Lennard-Jones radius for Se (4.0 Å) compared to that of C and N. The $SeCN^-$ is treated as a rigid molecule, while the D_2O bonds and angles are fixed using the SHAKE algorithm.[43] This model was shown to give excellent agreement with the measured reorientational anisotropy from PSPP experiments in bulk D_2O.[22]

The silica pore model (Figure 1B) is based on those previously developed by Gulmen and Thompson.[44,45] In this approach, the pore is generated by first heating a simulation cell of crystalline SiO_2 to 8000 K to generate molten silica. A cylinder that interacts only through a Lennard-Jones potential is then slowly grown in the center of the simulation cell, displacing the liquid SiO_2 to form a pore. The simulation temperature is subsequently reduced to room temperature at a rate fast enough to prevent crystallization (e.g., 50 K/ps). This process results in an amorphous silica pore that is not functionalized. To provide the typical −OH termination of mesoporous silica, a hydrolysis reaction is simulated by choosing elongated Si−O bonds near the pore surface and adding an −OH to the Si and an H to the O atom; this procedure ensures charge neutrality in a straightforward way. Changing the parameters used to identify the Si−O bonds can modify the surface hydroxyl density. The pore model used in the present simulations is ∼2.4 nm in diameter with 2.5 OH/nm^2 (Figure 1B).

The interactions of the pore with the D_2O liquid and $SeCN^-$ solute are through Lennard-Jones and Coulombic interactions, with the parameters for the pore atoms given in Table 1 (O_b indicates a bridging, or siloxane, oxygen); Lorentz−Berthelot mixing rules were used. The pore atoms are held rigid except for the hydroxyls of the silanol, Si−OH, and geminal, $Si(OH)_2$, groups at the pore surface, for which bonds are held fixed by the SHAKE algorithm but bond and dihedral angles are flexible (Table 1). For the geminal groups, no intramolecular dihedral potential is used, but the 1−4 (O−Si−O−H) and 1−5 (H−O−Si−O−H) Lennard-Jones and Coulombic interactions are included, scaled by a factor of 0.5 and 1, respectively. The charges used in the present simulation are taken from the ClayFF model[46] and are larger in magnitude than those previously used to successfully simulate confined liquids,[45,47,48] including vibrational spectra.[49,50] This choice is derived from comparisons of the present simulation results and measurements (*vide infra*). The interactions were calculated with a cutoff of radius 12 Å, and the long-range electrostatics were accounted for with the damped-shifted force method[51] with a damping parameter of 0.2.

Table 1. Silica Pore Force Field Parameters

atom	(Å)	(kcal/mol)	(e)
Si	2.500	0.00010	2.10
O_b	2.700	0.45686	−1.05
O	3.070	0.16995	−0.95
H	1.295	0.00037	0.425
angle		k (kcal/mol/rad^2)	(deg)
Si−O−H		24.499325	118.5
HO−Si−OH		38.155673	118.5

The simulation was prepared by carrying out grand canonical Monte Carlo (GCMC) simulations in which water molecules are inserted and removed from the pore to equalize the chemical potential with that of bulk liquid water; this provides the equilibrium density in the pore corresponding to complete filling (100% RH). These GCMC calculations were completed using our previously developed pore charges.[44,45] The $SeCN^-$ solute was inserted by replacing one of the water molecules. This gives 448 water molecules and one solute in the pore. While this is a lower concentration than used in the experiments, both are in the dilute limit with no effect from interactions between solutes. Moreover, the K^+ counterion present in the experiments is not included because no effects of ion pairing, e.g., a blue-shifted shoulder in the linear-IR spectrum, were observed.[52,53] The results presented are obtained from ten 18 ns trajectories in the *NVT* ensemble

DOI: 10.1021/acs.jpcc.9b00593
J. Phys. Chem. C 2019, 123, 5790−5803

with the temperature maintained at 298 K by a Nosé−Hoover thermostat[54,55] with a time constant of 100 fs. The time step is 1 fs, and configurations are written every 12 fs following a 2.5 ns equilibration stage, with velocity rescaling used to maintain the temperature over the first 0.5 ns. Each trajectory differs in the initial velocities, randomly selected from a Boltzmann distribution. In most cases, error bars on MD-derived data were calculated from block averaging (with each of the 10 trajectories as a block) and are reported as 95% confidence intervals using the Student's *t*-distribution.[56] For multi-exponential fits, the errors in the amplitudes and time scales are reported as a single standard deviation from five blocks (each consisting of an average of two trajectories); this approach is adopted to address issues of heterogeneity, i.e., the sensitivity of the time correlation function decay to the fraction of time $SeCN^-$ spends in the interfacial layer in a given trajectory.

III.B. Spectroscopic Modeling. The vibrational spectra of the CN stretching mode of $SeCN^-$ were calculated using the empirical frequency map developed previously for simulations in bulk D_2O.[22] The map is based on density functional theory calculations of the vibrational frequency in clusters extracted from MD simulations in the bulk liquid. Each cluster is centered on the $SeCN^-$ solute with nine waters explicitly considered and remaining waters within 10 Å of the center-of-mass included as point charges. The field used in the map is that from all waters within this 10 Å distance using the SPC/E model charges.[42] The map parameters are given in Table 2 of ref 22; the frequency is found to vary linearly with the field.

In the confined environment, there is a contribution to the field from the pore atoms, and because the map is derived from $SeCN^-$ in bulk D_2O, there is a choice about how those contributions should be calculated. The results presented are based on using the charges for all atoms within 10 Å of the $SeCN^-$ center of mass, but we found only modest differences when the field from all pore atoms was used instead.

IV. RESULTS AND DISCUSSION

IV.A. Linear-IR Spectrum. The linear-IR spectra of $SeCN^-$ (CN stretch) in bulk D_2O (black solid curve) and D_2O confined in the silica pore (red solid curve) are compared in Figure 2. Nanoscale confinement has no effect on the band center and full width at half-maximum (fwhm), which are 2075 and 33 cm^{-1}, respectively, for both systems (Table 2). This result is analogous to the surprising invariance of the water OH stretch spectrum upon confinement in silica glasses with different pores sizes[5] and in MD simulations of water confined in a silica pore model similar to that used here.[10] The simulations revealed that the line shapes for OH groups rapidly approached the bulk spectrum as they moved only a small distance away from the surface, beginning at as little as 3 Å between the hydroxyl H atom and nearest pore O atom. In other words, only OH groups that were hydrogen bonded to the pore exhibited perturbed frequencies.

However, the enhanced absorption on the red edge of the bulk spectrum is absent in the confined spectrum (Figure 2). The asymmetric bulk line shape has been attributed to the frequency dependence of the CN transition dipole moment, μ_{01}, in D_2O, which results from the variation in H-bond number and strength across the line.[22] The disappearance of the red wing results in a symmetric line shape in the pore. Insight can be gained from the simulations by computing, in addition to the linear-IR absorption spectrum, the frequency distribution, $P(\omega) = \langle\delta(\omega - \omega_{01})\rangle$, and $P(\omega)$ weighted by the transition dipole moment squared, i.e., the spectral density, $P_\mu(\omega) = \langle|\mu_{01}|^2\delta(\omega - \omega_{01})\rangle$. The calculated quantities in the bulk liquid and silica pore systems are compared in Figure 3A. The simulated IR spectrum (blue curve) shows a minimal (<1 cm^{-1}) shift in the band center relative to that in bulk D_2O (black curve), in agreement with the measurements. However, the modeling predicts significant broadening of the spectrum relative to that in the bulk liquid, with a fwhm that is 60% larger (Table 2). This broadening appears to be a consequence of both greater heterogeneity in the distribution of CN frequencies (red dashed curve), as shown in Figure 3A, for which the fwhm increases by 30% relative to that in bulk D_2O (Table 2), and reduced motional narrowing. It is not fully clear in which of these aspects the modeling of the CN frequency is deficient, though based on the dynamical results below, it appears to be the former.

The simulated spectra can be calculated as a function of the $SeCN^-$ position in the pore, based on the distance of the C atom from the nearest pore O atom, d, at $t = 0$ in the calculation of the response function.[22] This is shown in Figure 3B. These results show a systematic red shift in the CN frequency as the molecule approaches the pore surface. At the same time, the line width increases as d decreases. At the largest distance from the pore wall, $d = 10$ Å, the spectrum is

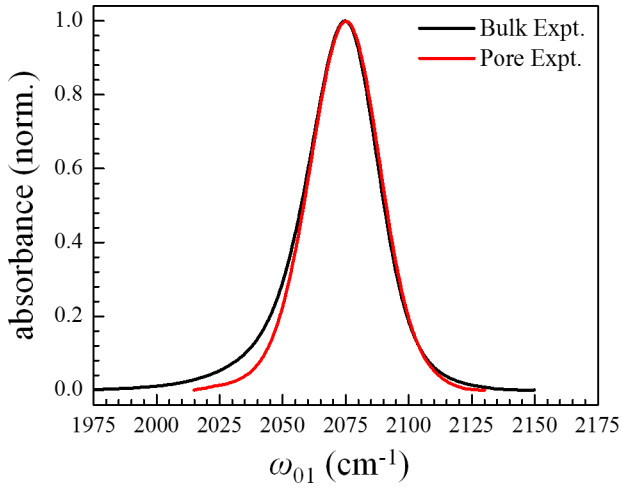

Figure 2. Linear-IR spectrum of $SeCN^-$ in bulk D_2O (black curve) and in D_2O confined in the silica pore (red curve). Broadening on the red side of the spectrum is noticeably diminished in the pore.

Table 2. Parameters for Line Shapes and Distributions[a]

	line shape/distribution	sample	center (cm^{-1})	fwhm (cm^{-1})
expt	$I(\omega)$	bulk	2074.7 ± 0.1	32.9 ± 0.1
		pore	2075.1 ± 0.7	32.6 ± 0.7
sim	$I(\omega)$	bulk	2075	38.5
		pore	2074	61
	$P(\omega)$	bulk	2077	59.6
		pore	2077	78
	$P_\mu(\omega)$	bulk	2072	58.8
		pore	2071	77

[a]Centers and fwhm's for the measured (expt) and simulated (sim) FT IR spectra, $I(\omega)$, frequency distributions, $P(\omega)$, and spectral densities, $P_\mu(\omega)$, for 0.3 M $SeCN^-/D_2O$ in bulk solution and confined in the silica pore. The parameters for the bulk liquid are reproduced from ref 22.

DOI: 10.1021/acs.jpcc.9b00593
J. Phys. Chem. C 2019, 123, 5790−5803

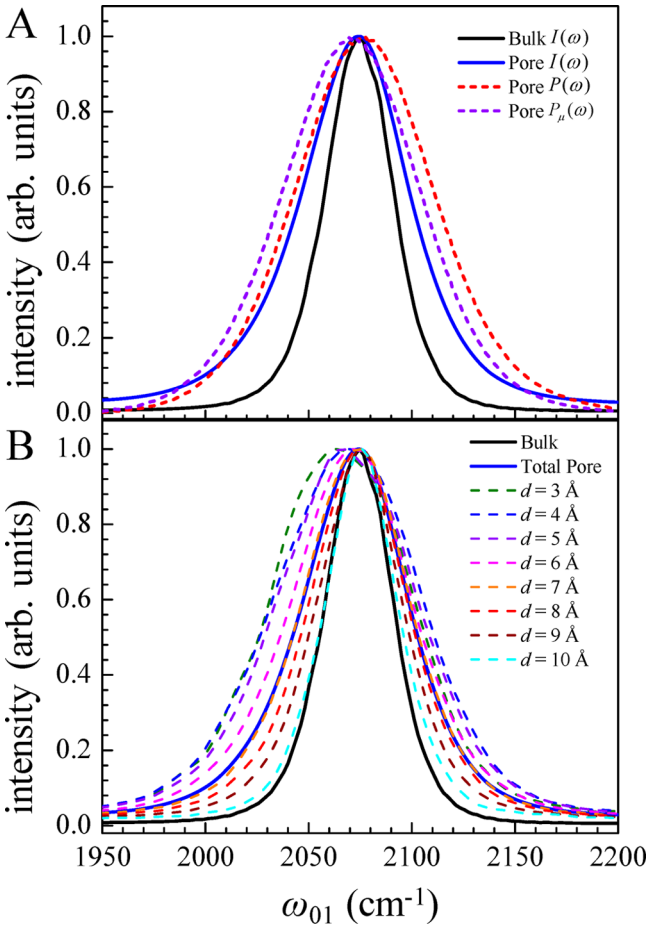

Figure 3. (A) Simulated linear-IR spectrum (blue curve), frequency distribution (red dashed curve), and spectral density (violet dashed curve) of $SeCN^-$ in D_2O confined in the silica pore; the simulated bulk IR spectrum (black curve) is shown for comparison. (B) Distance-dependent IR spectra (dashed curves) for $SeCN^-$ in D_2O confined in the pore are compared to the total pore (blue curve) and bulk (black curve) IR spectra.

close to that of $SeCN^-$ in bulk D_2O, exhibiting only a slightly broader line width.

We previously found that for $SeCN^-$ in bulk D_2O the effect of H-bond donors on the CN frequency could be divided into two classes. That is, axial H-bonds, taken to be when the C−N−D angle is more than 120°, induce a blue shift in the CN stretch. This effect is associated with charge transfer from the nitrile lone pair, which has some π^* antibonding character, to the OD bond.[49,57] Nonaxial, equatorial, H-bonds cause red shifts in the CN frequency. It is interesting then to compare how these effects are modified for $SeCN^-$ in silica-confined D_2O compared to the bulk liquid. This is shown in Figure 4, where the distributions of the two H-bond types and the average CN frequency as a function of the number of axial and total H-bonds are shown and compared to the bulk solution results.[22] The results in Figure 4A show that the distribution of axial H-bonds is only very slightly changed upon confinement while the pore does favor a smaller number of total H-bonds.

This is further examined in Figure 4B, where the average number of axial and total H-bonds is plotted as a function of distance from the pore wall. The average number of total H-bonds is smallest at the interface, d = 3 Å, and rises to a maximum of 3.25 at 5 Å before plateauing at 3.15 at larger d.

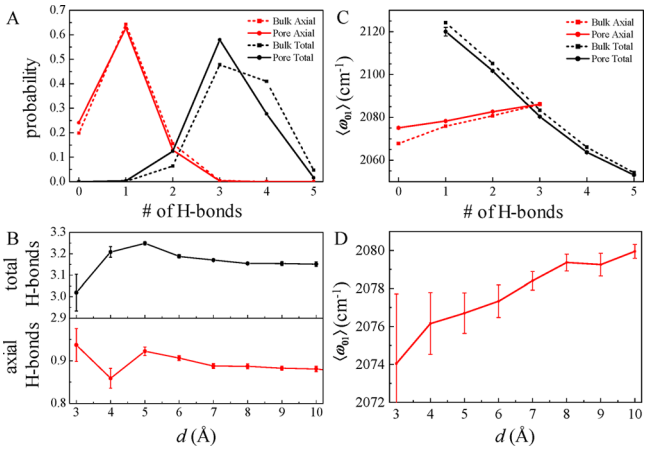

Figure 4. (A) Calculated probability of the total number of H-bonds donated to $SeCN^-$ by D_2O and silanols (black points) and the number of axial H-bonds (red points) defined as $\theta_{CND} \geq 120°$. Results in the silica pore (solid lines) are compared to those for the bulk solution (dashed lines). (B) Average number of total (black circles) and axial (red circles) H-bonds donated to $SeCN^-$ as a function of the C atom distance to the nearest pore O atom, d. (C) Averaged CN stretching frequency as a function of the number of total (black points) and axial (red points) H-bonds. Results in the pore (solid lines) are compared to those for the bulk solution (dashed lines). (D) Average CN stretching frequency as a function of d.

These values are slightly less than the average of 3.4 total H-bonds found in bulk D_2O. In contrast, the average number of axial H-bonds is largest next to the pore surface, oscillates between d = 4 and 5 Å, and converges to 0.88 at larger distances. This gives the overall average number of axial H-bonds in the pore as 0.89 compared to 0.97 in bulk solution. Thus, the simulations show that confinement slightly inhibits the formation of H-bonds.

The effect of the H-bonding arrangement on the CN stretching frequency is illustrated in Figure 4C, where the average frequency is plotted versus the number of axial and total H-bonds. The results are quite comparable to those found in bulk D_2O and consistent with the picture described above for the frequency shifts; i.e., increasing the number of axial H-bonds increases the CN frequency while a greater number of total H-bonds decreases it. For a given number of total (axial) H-bonds, $SeCN^-$ in the pore has a lower (higher) frequency compared to in the bulk solution. This suggests that the lack of a frequency shift in the IR spectrum upon confinement in silica pores results from the cancellation of different effects.

How the $SeCN^-$ position in the pore affects the vibrational frequency is examined in Figure 4D, where the average frequency is plotted as a function of the distance, d, from the nearest pore O atom. The frequency increases monotonically with d from 2074 cm^{-1} at d = 3 Å to 2080 cm^{-1} at d = 10 Å, though the change at small d is not well resolved due to the large uncertainties. This trend is not fully explained by the results in Figure 4B,C. The convolution of those results would suggest the transition frequency would be the largest at the interface, reach a minimum at d = 5 Å, and then increase with d thereafter; because the frequency is more sensitive to the total number of H-bonds, this is the dominant contribution. These differences suggest that the electrostatic environment at the interface cannot be understood solely in terms of H-bonding to the $SeCN^-$ anion.

DOI: 10.1021/acs.jpcc.9b00593
J. Phys. Chem. C 2019, 123, 5790−5803

IV.B. PSPP Spectroscopy: Orientational Relaxation. To analyze the orientational relaxation dynamics of the $SeCN^-$ anion in confined D_2O, the reorientational anisotropy was calculated from the PSPP signals with

$$r(t) = \frac{S_{\parallel}(t) - S_{\perp}(t)}{S_{\parallel}(t) + 2S_{\perp}(t)} \quad (2)$$

and from the simulations as

$$r(t) = \frac{2}{5}C_2(t) = \frac{2}{5}\langle P_2[\vec{e}(t)\cdot\vec{e}(0)]\rangle \quad (3)$$

where $C_2(t)$ is the orientational correlation function, P_2 is the second-order Legendre polynomial, $\vec{e}(t)$ is the transition dipole moment unit vector at time t, and $\langle ... \rangle$ represents an ensemble average. The measured (solid points) and simulated (solid curves) $r(t)$ are displayed in Figure 5A. It is important to note that the form of eq 2 is only strictly true for a 3D isotropic system.[58,59] Assuming an average spherical particle size of ~10 μm, we estimated that within the ~100 μm waist and ~25 μm focal depth of the incident infrared beams there are $>10^3$ particles that are randomly oriented. Therefore, the system can be regarded as macroscopically isotropic, and eq 2 can be used to extract $C_2(t)$.

The cylindrical pore structure of MCM41 may lead to a preferred orientation of $SeCN^-$, particularly near the silica surface. This possibility was addressed through the simulations by calculating the probability distribution of the $SeCN^-$ as a function of the C atom distance from the pore wall. This is shown in Figure 6 along with corresponding results for the water atoms. The results show that $SeCN^-$ is preferentially found away from the pore interface, with a broad distribution between d = ~3.5 and ~10 Å. This is a result of the strong affinity of water for the pore surface, which is indicated by the strongly peaked probability distributions for the water atoms at small d. At larger distances, the distributions for the water sites behave linearly, reflecting a uniform density convoluted with the linearly decreasing volume available as the pore center is approached. It is in this relatively unstructured water outside the interfacial layer that the $SeCN^-$ is predominantly located. Quantitatively, the interfacial water layer can be roughly defined as d < 4 Å, and the solute is outside of this region 95% of the time. Because of this preference for the center of the pore, the $SeCN^-$ has a nearly uniform angular distribution.

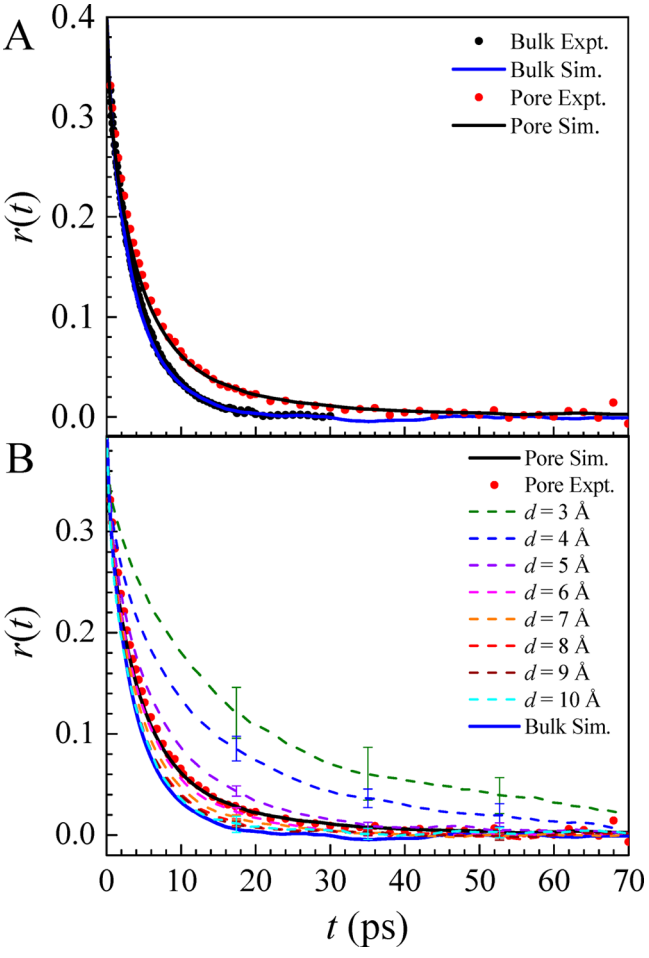

Figure 5. (A) Measured rotational anisotropy, $r(t)$, of $SeCN^-$ in bulk D_2O (black points) and in D_2O confined in the silica pore (red points) is compared to the simulation results for the bulk (blue curve) and pore systems (black curve). (B) Simulated $r(t)$ decomposed according to the distance between the C atom and nearest pore O atom, d. The measured pore data from (A) are also redisplayed for comparison.

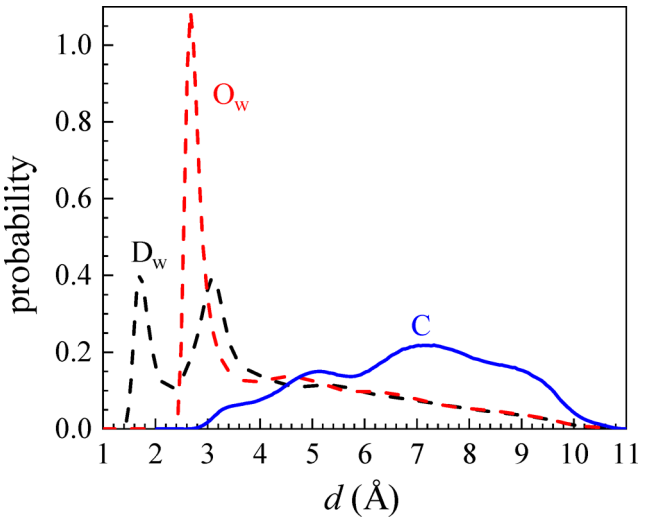

Figure 6. Probability distribution for the $SeCN^-$ carbon atom (blue curve) and D_2O oxygen (red dashed curve) and deuterium (black dashed curve) atoms.

In Figure 5A, it is seen that the calculated orientational relaxation in the simulated pore (black curve) agrees very well with the experimental measurements (red points). Excellent agreement was also obtained in the bulk case,[22] and those data (black points) are reproduced in Figure 5A for comparison. Clearly, reorientation of the $SeCN^-$ molecule slows significantly when confined in the pores of MCM41. As observed in the bulk liquid, $SeCN^-$ experiences motions that contribute to its orientational relaxation on time scales shorter than can be resolved in the present experiments employing 150 fs mid-IR pulses. The amplitude of the fast inertial fluctuations in $\vec{e}(t)$ can be assessed by summing the amplitudes of multi-exponential fits to the data (Table 3), which are associated with the observable dynamics, and calculating the deviation from 0.4 (eq 3). The amplitude of the inertial component is ~0.02 (within error) out of 0.4 total for both systems, representing a small contribution to the total orientational randomization. Thus, confinement perturbs the amplitudes

DOI: 10.1021/acs.jpcc.9b00593
J. Phys. Chem. C 2019, 123, 5790−5803

Table 3. Orientational Relaxation Parameters[a]

sample	A_1	t_1 (ps)	A_2	t_2 (ps)	A_3	t_3 (ps)	τ_c (ps)
bulk	0.073 ± 0.002	1.4 ± 0.1	0.304 ± 0.003	4.5 ± 0.1			3.8 ± 0.1
pore	0.11 ± 0.04	2.0 ± 0.4	0.24 ± 0.03	6.2 ± 0.9	0.03 ± 0.02	25 ± 8	6.3 ± 0.5
simulations bulk	0.10 ± 0.01	0.9 ± 0.1	0.29 ± 0.01	4.5 ± 0.1			3.5
simulations pore	0.10 ± 0.02	0.6 ± 0.1	0.26 ± 0.03	4.8 ± 1.0	0.05 ± 0.04	20 ± 10	5.9 ± 1.0

[a]Multiexponential fit parameters to the anisotropy for 0.3 M $SeCN^-/D_2O$ in bulk solution and confined in the silica pore. The A_i and t_i are the amplitude and time constant of the ith component. The τ_c are integrated correlation times (eq 4).

and time scales of the diffusive motions of the anion, which lead to significantly slower orientational relaxation.

A useful measure of the change in dynamics, which weights each time scale component by its normalized amplitude, is the integrated correlation time, defined by

$$\tau_c = \frac{1}{A(0)}\int_0^\infty A(t)\,dt \tag{4}$$

where $A(t)/A(0)$ represents a normalized correlation function, in this case $C_2(t)$. The integrated correlation time describing the reorientation of $SeCN^-$ is seen to increase by a factor of ~1.7 between the bulk (3.8 ps) and confined liquid (6.3 ps) (Table 3). This substantial slowing is remarkable considering the modest change in the linear-IR spectrum (Figure 2). Similar results have been obtained for neat water confined in mesoporous silica.[5,10] Namely, the IR spectrum in the OH stretching region was found, in both simulations and measurements, to be insensitive to confinement, while the same simulations show dramatically slowed, nonexponential reorientational dynamics. Because of the considerably shorter OH vibrational lifetime (compared to $SeCN^-$), the complete water orientational relaxation is not readily measured. The anisotropy decay of $SeCN^-$ in the silica pore (red solid points, Figure 5A) is described well with a triexponential fit (Table 3, row 3). The data show fast time scales with magnitudes and amplitudes similar to the bulk time scales (Table 3, row 2), although modestly slower. The major difference is a smaller amplitude, long time scale (t_3 = 25 ± 8) that is absent in the bulk liquid.

In Figure 5B, the simulated $SeCN^-$ anisotropy is decomposed according to the distance of the solute from the pore wall (defined by d, the C atom distance to the nearest pore O atom) at t = 0. These data show that the orientational relaxation is slowest directly near the surface and gradually accelerate as the molecule moves further into the center of the pore. This is most notable in the decay at longer times which, as noted above, exhibits significant retardation relative to that in the bulk liquid. The results in Figure 5B show that this is primarily associated with $SeCN^-$ molecules that are in the interfacial layer of the pore. However, the change in the rotational dynamics is continuous as a function of the $SeCN^-$ distance from the pore surface, distinct from the assumption of two-state, or core−shell, models. Indeed, $C_2(t)$ can be fit well to a triexponential form for all distances except the largest considered (d = 10 Å) where a biexponential fit is sufficient. It is interesting, however, that even at this distance the orientational relaxation is slightly slower than that in the bulk liquid, a result that is indicative of the small pore size.

It is interesting to further consider the distance dependence of $C_2(t)$ in the context of the typical models applied to confined liquids. Foremost among these is the two-state, or core−shell, model,[45,60−63] in which it is assumed that the property of interest in the interfacial layer (the "shell") is distinctly different than that in the pore interior (the "core"). Mathematically, it can be represented, for $C_2(t)$, as

$$C_{2,2st}(t;\,d) = C_{2,core}(t) + [C_{2,shell}(t) - C_{2,core}(t)]\theta(\Delta - d) \tag{5}$$

where $C_{2,core}(t)$ and $C_{2,shell}(t)$ are the orientational correlation functions characteristic of the interior and interfacial regions, respectively, Δ is the width of the interfacial layer, and θ is the Heaviside step function. It can be seen from Figure 5B that this does not even qualitatively describe the distance dependence of the orientational correlation function. The behavior of $C_2(t;d)$ with d is more quantitatively examined in Figure 7,

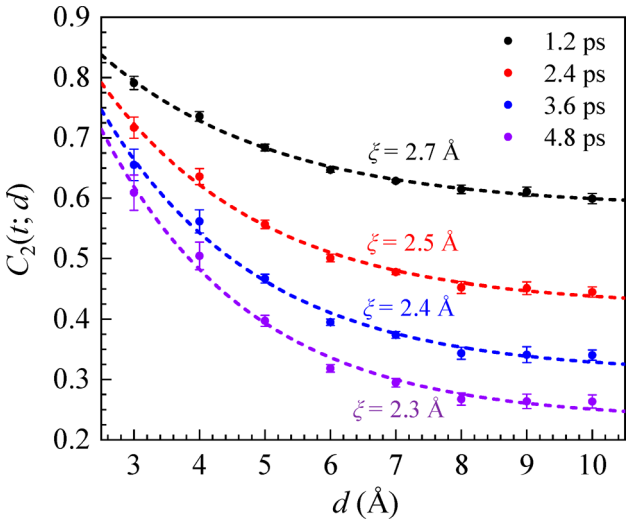

Figure 7. Simulated $C_2(t;d)$ as a function of the distance, d, between the C atom and nearest pore O atom evaluated at four delay times: 1.2 ps (black circles), 2.4 ps (red circles), 3.6 ps (blue circles), and 4.8 ps (violet circles). Dashed lines of the same color show fits to an exponential decay (eq 6).

where the values of $C_2(t;d)$ at particular times are plotted versus d. This behavior is clearly not that of a step function change from the interfacial layer to the core. Rather, as shown in Figure 7, the value at each time is well described by a decaying exponential

$$C_{2,exp}(t;\,d) = C_{2,core}(t) + [C_{2,shell}(t) - C_{2,core}(t)]e^{-(d-d_0)/\xi} \tag{6}$$

where d_0 is a reference distance taken to be 3 Å. However, these exponential fits yield different values of the length scale, ξ, for each time. The change in ξ is ~20%. This change reflects the multiexponential time dependence of $C_2(t)$ and indicates that the distance dependence for each amplitude and time scale is not the same.

The results presented here are consistent with results on small reverse micelles.[63] The core−shell model provides a

DOI: 10.1021/acs.jpcc.9b00593
J. Phys. Chem. C 2019, 123, 5790−5803

reasonable description of water orientational relaxation dynamics for large reverse micelles, in which the diameter of the water nanopool is greater than ~6 nm. For large reverse micelles, the water in the core displays bulk water dynamics and bulk IR spectra of the hydroxyl stretching mode. Water molecules directly interacting with the interface show substantially different spectra and dynamics than the bulk-like water core.[63] However, even for large reverse micelles with a substantial bulk water center, there is a transition region between the interfacial dynamics and the bulk dynamics of the core.[64] For reverse micelles with water nanopools less than ~4 nm, orientational relaxation measurements display no evidence of a distinct core. Like the experiments presented here, for small reverse micelles the data cannot be separated into core and shell components.[63] However, simulations show that there is a change in the dynamics as the distance from the interface increases.[65] The size of the nanopores studied here is in the range of the size of the water nanopools in reverse micelles that do not fit the core−shell model.

IV.C. 2D IR Spectroscopy: Spectral Diffusion. Nanoscale confinement in porous silica results in a significant change in the collective and single molecule orientational relaxation of water.[1,6−9] Thus, it is also anticipated to have a large influence on the rearrangement of the water H-bond network. The time scales of these motions in bulk water have been the focus of many experimental[20,66,67] and theoretical[66,68] studies. However, direct study of water in the context of nanometer-size silica pores with nonlinear-IR spectroscopy has been limited by its short-lived vibrationally excited state, which prevents observation of the slower dynamics occurring in the confined environment.[21,69] Furthermore, scattered light from the silica framework poses a nontrivial challenge to acquire and extract reliable time-dependent line shapes from mesoporous silica powders.

The spectral diffusion of $SeCN^-$ in D_2O was recently analyzed in detail[22] and shown to be remarkably similar to the measured spectral diffusion of HOD in D_2O. Water spectral diffusion is characterized by two main time scales.[20,66] The first (~0.4 ps) originates from structural fluctuations associated with local H-bond configurations. The final time scale (~1.4 ps), which is within error, the same for HOD and $SeCN^-$, is associated with the concerted intermolecular rearrangements that randomize the H-bond network around the probe. The rotational dynamics of the $SeCN^-$ molecule were also shown to contribute negligibly to its own spectral diffusion[22] through the absence of reorientation induced spectral diffusion (RISD).[70,71] $SeCN^-$ spectral diffusion in water is therefore mainly determined by H-bond network structural dynamics.

To quantify the nature of water H-bond dynamics in MCM41, measurements and simulations of $SeCN^-$ spectral diffusion were performed in the water-filled silica pores. The full range of dynamics were measured with complete removal of scatter by acquiring spectra in an $\langle XXYY \rangle$ configuration with a four-shot phase cycle sequence.[25] Representative spectra for T_w = 0.5 ps and T_w = 30 ps are shown in Figure 8. A clear change in the shape of the 0 → 1 transition (red, positive going peak) is observed as spectral diffusion proceeds with increasing T_w. The time-dependent 0 → 1 band shape was analyzed using the center-line-slope (CLS) method[39,40] as was described for $SeCN^-$ in D_2O.[22] The CLS decay is shown (red points) in Figure 9 alongside the data for the bulk system (black points) reproduced from the previously published study.[22] Consistent with predictions,[10] the H-bond network dynamics in the silica

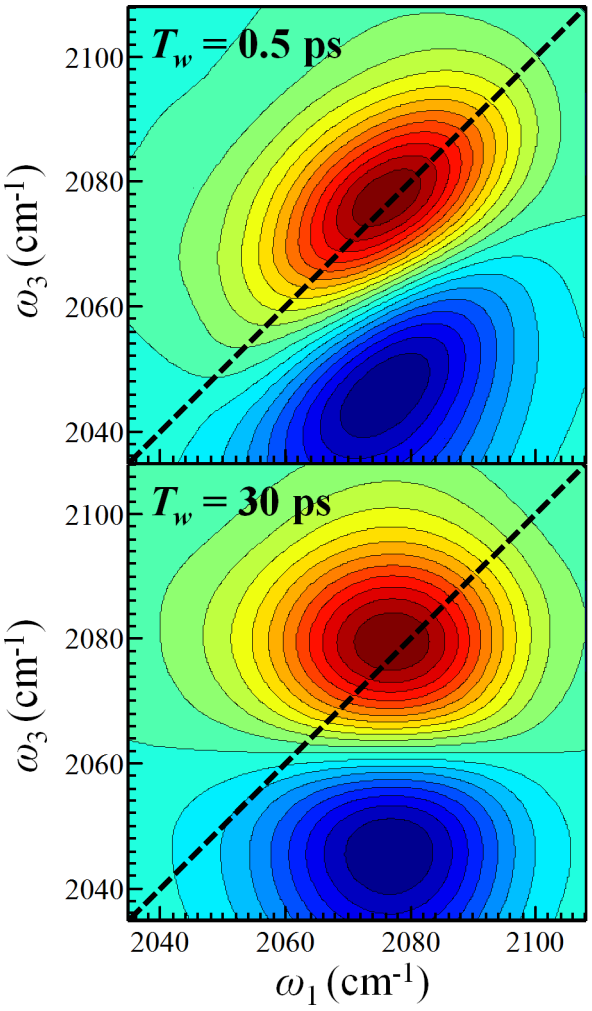

Figure 8. Measured 2D IR spectra of $SeCN^-$ in D_2O confined in the silica pore. The spectrum is noticeably rounder and less tilted at the longer waiting time (T_w = 30 ps), indicating that spectral diffusion is more complete.

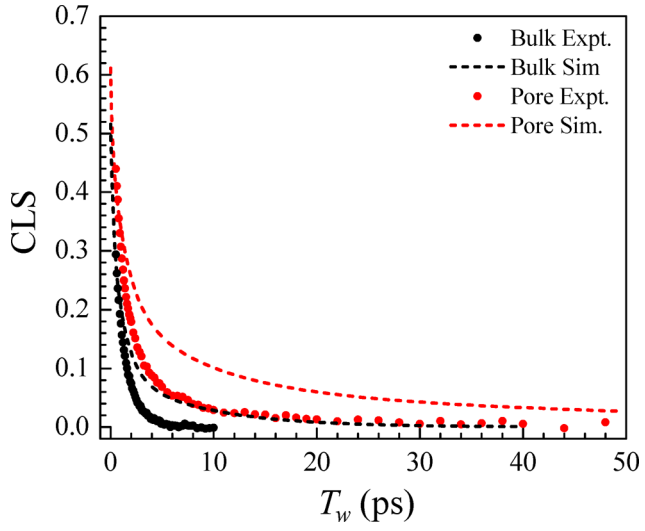

Figure 9. CLS decays (spectral diffusion) of $SeCN^-$ in D_2O (black points) and in D_2O confined in the silica pore (red points). The respective simulated CLS decays are shown as dashed lines of the same color.

DOI: 10.1021/acs.jpcc.9b00593
J. Phys. Chem. C 2019, 123, 5790−5803

Table 4. CLS Parameters[a]

sample	A_1	τ_1 (ps)	A_2	τ_2 (ps)	A_3	τ_3 (ps)	τ_c (ps)
bulk	0.22 ± 0.02	0.5 ± 0.1	0.30 ± 0.04	1.3 ± 0.2			0.97 ± 0.05
pore	0.49 ± 0.05	0.8 ± 0.2	0.19 ± 0.02	3.1 ± 0.3	0.04 ± 0.01	17 ± 1	2.4 ± 0.3
simulations bulk	0.27 ± 0.01	0.6	0.11 ± 0.01	1.4	0.11 ± 0.01	6.9 ± 0.2	2.3
simulations pore	0.28 ± 0.01	1.7 ± 0.5	0.15 ± 0.01	10 ± 5	0.06 ± 0.01	60 ± 35	8.5

[a]Multiexponential fit parameters to the CLS for $SeCN^-/D_2O$ in bulk solution and confined in the silica pore. The A_i and τ_i are the amplitude and correlation time constant of the ith component. The τ_c are integrated correlation times (eq 4).

Table 5. FFCF Parameters[a]

sample	T_2 (ps)	Γ (cm^{-1})	Δ_1 (cm^{-1})	τ_1 (ps)	Δ_2 (cm^{-1})	τ_2 (ps)	Δ_3 (cm^{-1})	τ_3 (ps)
bulk	1.4 ± 0.1	8.7 ± 0.4	9.4 ± 0.5	0.5 ± 0.1	10.2 ± 0.9	1.3 ± 0.2		
pore	2.3 ± 0.6	5 ± 1	12.2 ± 0.7	0.8 ± 0.2	6.8 ± 0.5	3.1 ± 0.3	3.1 ± 0.3	17 ± 1

sample	Δ_0 (cm^{-1})	τ_0 (ps)	Δ_1 (cm^{-1})	τ_1 (ps)	Δ_2 (cm^{-1})	τ_2 (ps)	Δ_3 (cm^{-1})	τ_3 (ps)
simulations bulk	19.0 ± 0.1	0.089 ± 0.001	13.2 ± 0.1	0.6	6.0 ± 0.1	1.4	5.6 ± 0.1	7.1 ± 0.1
simulations pore	29.8 ± 0.9	0.157 ± 0.010	16.9 ± 1.0	1.7 ± 0.5	11.6 ± 1.5	10 ± 5	7.1 ± 2.6	60 ± 35

[a]See section IV.C for parameter definitions.

pore are substantially slower than in bulk D_2O. The integrated correlation time (eq 4), τ_c, slows from 0.97 ps (bulk) to 2.4 ps (pore) (Table 4). The results indicate that deceleration of water structural relaxation around $SeCN^-$ (~2.5-fold, Table 4) is more substantial than deceleration of $SeCN^-$ reorientation (~1.7-fold, Table 3) between the confined and bulk liquid.

In a manner consistent with the behavior of $SeCN^-$ reorientation in the silica pore, the time scales of the fast spectral diffusion components, τ_1 and τ_2, are analogous to the bulk spectral diffusion (Table 4). The significant change is the appearance of an additional slow spectral diffusion component in the pore, $\tau_3 = 17 \pm 1$ ps, which is absent in the bulk liquid and more than an order of magnitude longer than any time scale observed in the bulk system. The spectral diffusion comparison is consistent with a picture of dramatically slower H-bonding dynamics near the silica surface and faster dynamics further away, which are still slower than in bulk water.

The measured CLS and linear absorption line shape were used to obtain the frequency–frequency correlation function (FFCF).[39,40] The FFCF was modeled with the Kubo ansatz[37]

$$\mathrm{FFCF} = C_\omega(t)\langle\delta\omega(0)^2\rangle = \langle\delta\omega(t)\delta\omega(0)\rangle = \sum_i \Delta_i^2 \exp[-t/\tau_i] \tag{7}$$

where $C_\omega(t)$ is the normalized FFCF and the frequency fluctuation, $\delta\omega(t) = \omega(t) - \langle\omega\rangle$, is the difference between the probe's instantaneous and average frequency, $\omega(t)$ and $\langle\omega\rangle$, respectively. The ith component of the FFCF is characterized by a frequency fluctuation amplitude, Δ_i, and time constant, τ_i. Components in the homogeneous limit satisfy $\Delta_i\tau_i \ll 1$.[37,39,40] In this case, Δ_i and τ_i cannot be independently determined. In the homogeneous limit, the Kubo line shape function[37,39,40] generates a Lorentzian whose width $\Gamma^* = \Delta^2\tau/\pi = 1/\pi T_2^*$ is narrower than the frequency distribution ($\Delta^2\tau/\pi \ll \Delta$, motionally narrowed) and inversely proportional to the pure dephasing time, T_2^*. The observed homogeneous dephasing time is more precisely $(T_2)^{-1} = (T_2^*)^{-1} + (2T_1)^{-1} + (3T_{or})^{-1}$, where T_1 and T_{or} are the vibrational and orientational relaxation times, respectively.[39] Components with $\Delta_i\tau_i \gg 1$ are in the inhomogeneous limit.[37,39,40] In this limit, Δ_i is the standard deviation of the ith Gaussian component, and the total inhomogeneous line width is given by convolution: fwhm $= 2[2\ln(2)]^{1/2}\Delta_{total}$, where $\Delta_{total} = (\sum_i\Delta_i^2)^{1/2}$. The convolution of the line shapes associated with each component in eq 7 produces the linear (1D) absorption line shape. The correct FFCF will reproduce the linear absorption line shape and the CLS decay and is confirmed by reproducing the observables through response function calculations[37,39,40] of the 1D and 2D line shapes. The FFCF parameters obtained from the spectra in Figure 2 and corresponding CLS decays in Figure 9 are provided in Table 5.

The simulated CLS (dashed red curve), obtained from the simulations as previously described,[22] is compared to the measured results in Figure 9 along with that previously obtained for $SeCN^-$ in bulk D_2O (dashed black curve). The simulations, in agreement with the experimental data, find that the confinement leads to the appearance of an additional long time scale, beyond those observed in bulk solution, that is estimated to be ~60 ps but with significant uncertainty. This time scale is ~3 times longer than that observed in the measurement, indicating that the simulation modeling of the frequency is reasonable but could be improved. However, the frequency map used is linear so that the normalized FFCF obtained is independent of the map parameters and equal to the autocorrelation function of the electric field at the C atom along the $SeCN^-$ axis. Thus, in this description, the FFCF is determined by the dynamics of those electrostatic fluctuations in the solute environment, even when the frequency is not quantitatively modeled.

The distance dependence of the FFCF, $C_\omega(T_w)$, is shown in Figure 10A. It shows qualitatively different behavior than that of the orientational correlation function in Figures 5B and 7, namely the FFCFs for distances near the interface do not differ much but are distinct from those obtained when the solute is in the pore interior. This is suggestive of two-state behavior as expressed in eq 5. This is verified by examining the dependence of the FFCF on the position of the $SeCN^-$ in the pore at short times, which is shown in Figure 10B. Indeed, the distance-dependent FFCF behaves as a (smoothed) Heaviside step function, which can be seen by the agreement with fitting to the function

DOI: 10.1021/acs.jpcc.9b00593
J. Phys. Chem. C 2019, 123, 5790−5803

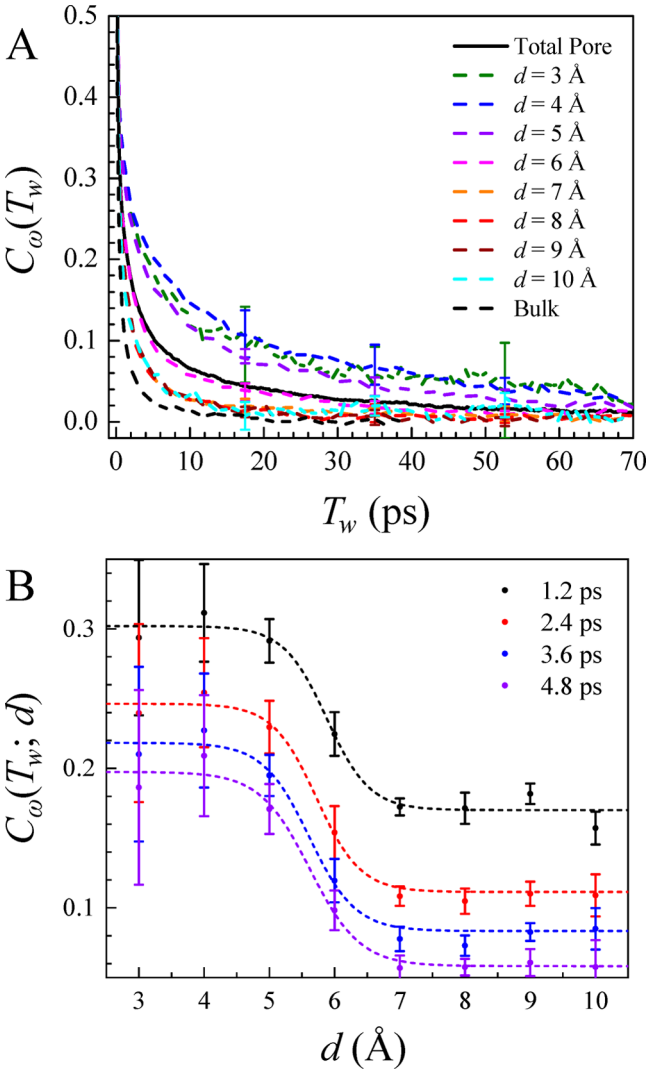

Figure 10. (A) Simulated FFCF as a function of the distance, d, between the C atom and nearest pore O atom (dashed curves) compared to the total pore (black solid curve) and bulk solution (black dashed curve) results. (B) Simulated FFCF evaluated at four delay times: 1.2 ps (black circles), 2.4 ps (red circles), 3.6 ps (blue circles), and 4.8 ps (violet circles). Dashed lines of the same color show fits to a smoothed step function (eq 8).

$$C_\omega(t; d) = C_{\omega,\mathrm{core}}(t) + [C_{\omega,\mathrm{shell}}(t) - C_{\omega,\mathrm{core}}(t)] \times \frac{\tanh[\{\Delta + d_0 - d\}/\alpha] + 1}{2} \quad (8)$$

where d_0 is taken as 3 Å and α is a fitting parameter that governs the smoothness of the step function. This qualitative difference in the distance dependence of the FFCF compared to the orientational correlation function is striking. It indicates that the spectral diffusion is governed by relatively local interactions, while $SeCN^-$ reorientation is influenced by more long-range effects. This is consistent with the bulk dynamics,[22] where the FFCF is observed to decay on a time scale of 1.3 ps, which is faster than that of 4.5 ps found for reorientation and also more rapid than the established time scale of ~3 ps for H-bond exchanges in water.[72] This demonstrates that the FFCF and $C_2(t)$ are probing different aspects of the H-bond dynamics.

V. CONCLUDING REMARKS

The detailed nature of water H-bond dynamics in MCM41 was elucidated by combining measurements and simulations of $SeCN^-$ vibrational spectroscopy in the water-filled ~2.4 nm silica pores. The study of $SeCN^-$ as a vibrational probe in the IR experiments offers several advantages over probing water directly. Foremost among these are the strong transition dipole and long vibrational lifetime of the CN stretching mode, which together permit the observation of complete rotational and spectral diffusion dynamics with high signal-to-noise. The combination of selecting smaller silica particles, index matching the sample, and implementing a new phase-cycling procedure aided in eliminating artifacts due to light scattering from the observables.

The simulated dynamics in a model silica pore were compared to the measured TCFs which, in contrast to the simulations, contain no spatial information. Comparisons of the spatially integrated dynamics from the simulations to the measured TCFs informed further adjustments to the pore model, leading to improved agreement with the measured dynamics. A new decay component was observed in both the rotational and spectral diffusion TCFs, $C_2(t)$ and $C_\omega(t)$, which in each case was significantly slower than the longest time scales in the bulk liquid (~6-fold and ~13-fold slower, respectively). These results indicate that the water H-bond dynamics are considerably perturbed upon confinement in the silica pore. On average, $SeCN^-$ forms slightly fewer H-bonds in the hydrated pore (3.2) than in bulk water (3.4). This appears to be related to the strong affinity of water for the hydroxyl-terminated pore, which results in increased water layering near the surface. In response to this interfacial solvent structuring, $SeCN^-$ tends to avoid the interfacial water (d < 4 Å) and resides in the more uniform water in the pore interior. However, the retarded solvent dynamics propagate out from the surface into the center of the pore, in turn dramatically slowing reorientation and spectral diffusion of $SeCN^-$ relative to bulk solution. This suggests that the significantly retarded dynamics observed in this system are likely modest compared to that in the interfacial layer, a conclusion that is supported by the distance dependence of the dynamics observed in the simulations. In the future, the interfacial dynamics might be more directly probed in experiments using solutes that possess a greater affinity for the silica surface.

Further analysis of the simulated TCFs revealed an unexpected difference in the evolution of $C_2(t)$ and $C_\omega(t)$ with distance from the pore surface. The $C_2(t)$ dynamics accelerate exponentially with distance from the surface, indicating that the orientational relaxation cannot be separated into distinct "core" and "shell" states for the small pore diameter studied here.[73,74] This is consistent with studies on very small water nanopools in reverse micelles.[63,65] In contrast, the $C_\omega(t)$ dynamics do transition as a (smoothed) step function from slower "shell" dynamics to accelerated "core" dynamics, in agreement with one of the conditions of a two-state model. The point of transition occurs at $d \simeq 6$ Å, halfway between the surface and center of the pore. This behavior indicates that the H-bonding degrees of freedom that couple to the vibrational frequency fall off more rapidly with distance than those which influence reorientation. It is important to note, however, that bulk spectral diffusion dynamics do not appear to exist in the "core" region, which is in opposition to a common secondary assumption of two-state models.

DOI: 10.1021/acs.jpcc.9b00593
J. Phys. Chem. C 2019, 123, 5790−5803

In conclusion, this work has shown that water experiences a range of structural and dynamic changes, some subtle and others substantial, upon confinement in nanoscale silica pores. The qualitatively different distance dependence observed for orientational relaxation and spectral diffusion, two properties sensitive to the H-bond dynamics of the confined water, revealed unexpected spatial complexity. Although considerable detail has been illuminated, certain aspects of this system remain incompletely described. In this study, the simulations quantitatively reproduced the measured orientational relaxation dynamics, but the agreement obtained for the spectral diffusion was not as good. Identifying properties of the simulation that lead to the overestimation of inhomogeneous broadening in the pore, as well as the time scales of the vibrational frequency fluctuations, will inform the modeling of H-bond dynamics in a broad range of mesoscopic systems; for instance, aqueous solutions in the crowded intracellular environment.[75] Therefore, the influence of surface properties such as roughness, charge, and hydroxyl density on the formation of H-bonds and their dynamics merits further systematic study. Another fundamental problem concerns the influence of pore size on the TCFs and their dependence on distance from the pore surface. Finally, work linking these detailed confinement effects to the operation of mesoporous silica in the fields of catalysis and energy may open new avenues for the directed design and application of these materials.

■ ASSOCIATED CONTENT

Supporting Information

The Supporting Information is available free of charge on the ACS Publications website at DOI: 10.1021/acs.jpcc.9b00593.

Experimental details; Figures S1−S4 and Tables S1−S3 (PDF)

■ AUTHOR INFORMATION

Corresponding Authors

*Phone 650 723-4446; e-mail fayer@stanford.edu.
*Phone 785 864-3980; e-mail wthompson@ku.edu.

ORCID

Ward H. Thompson: 0000-0002-3636-6448
Michael D. Fayer: 0000-0002-0021-1815

Notes

The authors declare no competing financial interest.

■ ACKNOWLEDGMENTS

This work was funded by the Division of Chemical Sciences, Geosciences, and Biosciences, Office of Basic Energy Sciences of the U.S. Department of Energy through Grant DE-FG03-84ER13251 (S.A.Y., J.Y.S, and M.D.F.) and the NSF-EPA Networks for Sustainable Design and Synthesis (NSMDS) for funding support under NSF Grant CHE-1339661 (W.H.T.). Additional support of the 2D IR instrument and for M.D.F. was provided by Air Force Office of Scientific Research Grant FA9550-16-1-0104. S.A.Y. acknowledges the support from a Stanford Graduate Fellowship. The simulations were performed at the University of Kansas Center for Research Computing (CRC). We thank Jun Nishida for his constructive comments on the manuscript.

■ REFERENCES

(1) Scodinu, A.; Fourkas, J. T. Comparison of the Orientational Dynamics of Water Confined in Hydrophobic and Hydrophilic Nanopores. *J. Phys. Chem. B* **2002**, *106*, 10292−10295.
(2) Faraone, A.; Liu, L.; Mou, C.-Y.; Shih, P.-C.; Copley, J. R. D.; Chen, S.-H. Translational and Rotational Dynamics of Water in Mesoporous Silica Materials: MCM-41-S and MCM-48-S. *J. Chem. Phys.* **2003**, *119*, 3963−3971.
(3) Faraone, A.; Liu, L.; Mou, C.-Y.; Yen, C.-W.; Chen, S.-H. Fragile-to-Strong Liquid Transition in Deeply Supercooled Confined Water. *J. Chem. Phys.* **2004**, *121*, 10843−10846.
(4) Takahara, S.; Sumiyama, N.; Kittaka, S.; Yamaguchi, T.; Bellissent-Funel, M.-C. Neutron Scattering Study on Dynamics of Water Molecules in MCM-41. 2. Determination of Translational Diffusion Coefficient. *J. Phys. Chem. B* **2005**, *109*, 11231−11239.
(5) Musat, R.; Renault, J. P.; Candelaresi, M.; Palmer, D. J.; Le Caër, S.; Righini, R.; Pommeret, S. Finite Size Effects on Hydrogen Bonds in Confined Water. *Angew. Chem., Int. Ed.* **2008**, *47*, 8033−8035.
(6) Milischuk, A. A.; Ladanyi, B. M. Structure and Dynamics of Water Confined in Silica Nanopores. *J. Chem. Phys.* **2011**, *135*, 174709.
(7) Laage, D.; Thompson, W. H. Reorientation Dynamics of Nanoconfined Water: Power-Law Decay, Hydrogen-Bond Jumps, and Test of a Two-State Model. *J. Chem. Phys.* **2012**, *136*, 044513.
(8) Milischuk, A. A.; Ladanyi, B. M. Polarizability Anisotropy Relaxation in Nanoconfinement: Molecular Simulation Study of Water in Cylindrical Silica Pores. *J. Chem. Phys.* **2014**, *141*, 18C513.
(9) Fogarty, A. C.; Duboué-Dijon, E.; Laage, D.; Thompson, W. H. Origins of the Non-Exponential Reorientation Dynamics of Nanoconfined Water. *J. Chem. Phys.* **2014**, *141*, 18C523.
(10) Burris, P. C.; Laage, D.; Thompson, W. H. Simulations of the Infrared, Raman, and 2D-IR Photon Echo Spectra of Water in Nanoscale Silica Pores. *J. Chem. Phys.* **2016**, *144*, 194709.
(11) Alarcos, N.; Cohen, B.; Ziółek, M.; Douhal, A. Photochemistry and Photophysics in Silica-Based Materials: Ultrafast and Single Molecule Spectroscopy Observation. *Chem. Rev.* **2017**, *117*, 13639−13720.
(12) Minakata, S.; Komatsu, M. Organic Reactions on Silica in Water. *Chem. Rev.* **2009**, *109*, 711−724.
(13) Gallo, P.; Rovere, M.; Chen, S. H. Dynamic Crossover in Supercooled Confined Water: Understanding Bulk Properties through Confinement. *J. Phys. Chem. Lett.* **2010**, *1*, 729−733.
(14) Bolis, V.; Fubini, B.; Marchese, L.; Martra, G.; Costa, D. Hydrophilic and Hydrophobic Sites on Dehydrated Crystalline and Amorphous Silicas. *J. Chem. Soc., Faraday Trans.* **1991**, *87*, 497−505.
(15) Chen, J.; Li, Q.; Xu, R.; Xiao, F. Distinguishing the Silanol Groups in the Mesoporous Molecular Sieve MCM-41. *Angew. Chem., Int. Ed. Engl.* **1996**, *34*, 2694−2696.
(16) Grünberg, B.; Emmler, T.; Gedat, E.; Shenderovich, I.; Findenegg, G. H.; Limbach, H. H.; Buntkowsky, G. Hydrogen Bonding of Water Confined in Mesoporous Silica MCM-41 and SBA-15 Studied by 1H Solid-State NMR. *Chem. - Eur. J.* **2004**, *10*, 5689−5696.
(17) Gierada, M.; Petit, I.; Handzlik, J.; Tielens, F. Hydration in Silica Based Mesoporous Materials: A DFT Model. *Phys. Chem. Chem. Phys.* **2016**, *18*, 32962−32972.
(18) Huber, C. J.; Massari, A. M. Characterizing Solvent Dynamics in Nanoscopic Silica Sol−Gel Glass Pores by 2D-IR Spectroscopy of an Intrinsic Vibrational Probe. *J. Phys. Chem. C* **2014**, *118*, 25567−25578.
(19) Huber, C. J.; Egger, S. M.; Spector, I. C.; Juelfs, A. R.; Haynes, C. L.; Massari, A. M. 2D-IR Spectroscopy of Porous Silica Nanoparticles: Measuring the Distance Sensitivity of Spectral Diffusion. *J. Phys. Chem. C* **2015**, *119*, 25135−25144.
(20) Fecko, C. J.; Eaves, J. D.; Loparo, J. J.; Tokmakoff, A.; Geissler, P. L. Ultrafast Hydrogen-Bond Dynamics in the Infrared Spectroscopy of Water. *Science* **2003**, *301*, 1698−1702.

DOI: 10.1021/acs.jpcc.9b00593
J. Phys. Chem. C 2019, 123, 5790−5803

(21) Park, S.; Fayer, M. D. Hydrogen Bond Dynamics in Aqueous NaBr Solutions. *Proc. Natl. Acad. Sci. U. S. A.* **2007**, *104*, 16731−16738.
(22) Yamada, S. A.; Thompson, W. H.; Fayer, M. D. Water-Anion Hydrogen Bonding Dynamics: Ultrafast IR Experiments and Simulations. *J. Chem. Phys.* **2017**, *146*, 234501.
(23) Rezus, Y. L. A.; Bakker, H. J. On the Orientational Relaxation of HDO in Liquid Water. *J. Chem. Phys.* **2005**, *123*, 114502.
(24) Spector, I. C.; Olson, C. M.; Huber, C. J.; Massari, A. M. Simple Fully Reflective Method of Scatter Reduction in 2D-IR Spectroscopy. *Opt. Lett.* **2015**, *40*, 1850−1852.
(25) Nishida, J.; Tamimi, A.; Fei, H.; Pullen, S.; Ott, S.; Cohen, S. M.; Fayer, M. D. Structural Dynamics Inside a Functionalized Metal−Organic Framework Probed by Ultrafast 2D IR Spectroscopy. *Proc. Natl. Acad. Sci. U. S. A.* **2014**, *111*, 18442−18447.
(26) Shim, S.-H.; Strasfeld, D. B.; Fulmer, E. C.; Zanni, M. T. Femtosecond Pulse Shaping Directly in the Mid-IR using Acousto-Optic Modulation. *Opt. Lett.* **2006**, *31*, 838−840.
(27) Shim, S.-H.; Zanni, M. T. How to turn your Pump-Probe Instrument into a Multidimensional Spectrometer: 2D IR and Vis Spectroscopies via Pulse Shaping. *Phys. Chem. Chem. Phys.* **2009**, *11*, 748−761.
(28) Kumar, S. K. K.; Tamimi, A.; Fayer, M. D. Comparisons of 2D IR Measured Spectral Diffusion in Rotating Frames using Pulse Shaping and in the Stationary Frame using the Standard Method. *J. Chem. Phys.* **2012**, *137*, 184201.
(29) Bohren, C. F.; Huffman, D. R. In *Absorption and Scattering of Light by Small Particles*; Bohren, C. F., Huffman, D. R., Eds.; Wiley-VCH Verlag GmbH & Co. KGaA: Weinheim, 2007.
(30) Brunauer, S.; Emmett, P. H.; Teller, E. Adsorption of Gases in Multimolecular Layers. *J. Am. Chem. Soc.* **1938**, *60*, 309−319.
(31) Barrett, E. P.; Joyner, L. G.; Halenda, P. P. The Determination of Pore Volume and Area Distributions in Porous Substances. I. Computations from Nitrogen Isotherms. *J. Am. Chem. Soc.* **1951**, *73*, 373−380.
(32) Kruk, M.; Jaroniec, M.; Sayari, A. Adsorption Study of Surface and Structural Properties of MCM-41 Materials of Different Pore Sizes. *J. Phys. Chem. B* **1997**, *101*, 583−589.
(33) Kruk, M.; Jaroniec, M.; Sakamoto, Y.; Terasaki, O.; Ryoo, R.; Ko, C. H. Determination of Pore Size and Pore Wall Structure of MCM-41 by Using Nitrogen Adsorption, Transmission Electron Microscopy, and X-ray Diffraction. *J. Phys. Chem. B* **2000**, *104*, 292−301.
(34) Kou, Y.; Schmidt, S. J. Vapor Pressure and Water Activity Measurements of Saturated Salt Solutions Made with D_2O at 20°C. *Food Chem.* **1999**, *66*, 253−255.
(35) Kittaka, S.; Ishimaru, S.; Kuranishi, M.; Matsuda, T.; Yamaguchi, T. Enthalpy and Interfacial Free Energy Changes of Water Capillary Condensed in Mesoporous Silica, MCM-41 and SBA-15. *Phys. Chem. Chem. Phys.* **2006**, *8*, 3223−3231.
(36) Kocherbitov, V.; Alfredsson, V. Hydration of MCM-41 Studied by Sorption Calorimetry. *J. Phys. Chem. C* **2007**, *111*, 12906−12913.
(37) Hamm, P.; Zanni, M. T. *Concepts and Methods of 2D Infrared Spectroscopy*; Cambridge University Press: New York, 2011.
(38) Tokmakoff, A. Orientational Correlation Functions and Polarization Selectivity for Nonlinear Spectroscopy of Isotropic Media. I. Third Order. *J. Chem. Phys.* **1996**, *105*, 1−12.
(39) Kwak, K.; Park, S.; Finkelstein, I. J.; Fayer, M. D. Frequency-Frequency Correlation Functions and Apodization in Two-Dimensional Infrared Vibrational Echo Spectroscopy: A New Approach. *J. Chem. Phys.* **2007**, *127*, 124503.
(40) Kwak, K.; Rosenfeld, D. E.; Fayer, M. D. Taking Apart the Two-Dimensional Infrared Vibrational Echo Spectra: More Information and Elimination of Distortions. *J. Chem. Phys.* **2008**, *128*, 204505.
(41) Tan, H.-S.; Piletic, I. R.; Fayer, M. D. Polarization Selective Spectroscopy Experiments: Methodology and Pitfalls. *J. Opt. Soc. Am. B* **2005**, *22*, 2009−2017.
(42) Berendsen, H. J. C.; Grigera, J. R.; Straatsma, T. P. The Missing Term in Effective Pair Potentials. *J. Phys. Chem.* **1987**, *91*, 6269−6271.
(43) Ryckaert, J.-P.; Ciccotti, G.; Berendsen, H. J. C. Numerical integration of the cartesian equations of motion of a system with constraints: molecular dynamics of n-alkanes. *J. Comput. Phys.* **1977**, *23*, 327−341.
(44) Gulmen, T. S.; Thompson, W. H. Model Silica Pores with Controllable Surface Chemistry for Molecular Dynamics Simulations. *MRS Online Proc. Libr.* **2005**, *899*, 0899−N0806−0805.
(45) Gulmen, T. S.; Thompson, W. H. Testing a Two-state Model of Nanoconfined Liquids: Conformational Equilibrium of Ethylene Glycol in Amorphous Silica Pores. *Langmuir* **2006**, *22*, 10919−10923.
(46) Cygan, R. T.; Liang, J.-J.; Kalinichev, A. G. Molecular Models of Hydroxide, Oxyhydroxide, and Clay Phases and the Development of a General Force Field. *J. Phys. Chem. B* **2004**, *108*, 1255−1266.
(47) Norton, C. D.; Thompson, W. H. On the Diffusion of Acetonitrile in Nanoscale Amorphous Silica Pores. Understanding Anisotropy and the Effects of Hydrogen Bonding. *J. Phys. Chem. C* **2013**, *117*, 19107−19114.
(48) Norton, C. D.; Thompson, W. H. Reorientation Dynamics of Nanoconfined Acetonitrile: A Critical Examination of Two-State Models. *J. Phys. Chem. B* **2014**, *118*, 8227−8235.
(49) Morales, C. M.; Thompson, W. H. Simulations of Infrared Spectra of Nanoconfined Liquids: Acetonitrile Confined in Nanoscale, Hydrophilic Silica Pores. *J. Phys. Chem. A* **2009**, *113*, 1922−1933.
(50) Burris, P. C.; Laage, D.; Thompson, W. H. Simulations of the Infrared, Raman, and 2D-IR Photon Echo Spectra of Water in Nanoscale Silica Pores. *J. Chem. Phys.* **2016**, *144*, 194709.
(51) Fennell, C. J.; Gezelter, J. D. Is the Ewald Summation Still Necessary? Pairwise Alternatives to the Accepted Standard for Long-Range Electrostatics. *J. Chem. Phys.* **2006**, *124*, 234104.
(52) Park, S.; Ji, M.; Gaffney, K. J. Ligand Exchange Dynamics in Aqueous Solution Studied with 2DIR Spectroscopy. *J. Phys. Chem. B* **2010**, *114*, 6693−6702.
(53) Sun, Z.; Zhang, W.; Ji, M.; Hartsock, R.; Gaffney, K. J. Contact Ion Pair Formation between Hard Acids and Soft Bases in Aqueous Solutions Observed with 2DIR Spectroscopy. *J. Phys. Chem. B* **2013**, *117*, 15306−15312.
(54) Nose, S. A Molecular Dynamics Method for Simulations in the Canonical Ensemble. *Mol. Phys.* **1984**, *52*, 255−268.
(55) Hoover, W. G. Canonical Dynamics: Equilibrium Phase-Space Distributions. *Phys. Rev. A: At., Mol., Opt. Phys.* **1985**, *31*, 1695−1697.
(56) Shoemaker, D. P.; Garland, C. W.; Nibler, J. W. *Experiments in Physical Chemistry*; McGraw-Hill: New York, 1989.
(57) Reimers, J. R.; Hall, L. E. The Solvation of Acetonitrile. *J. Am. Chem. Soc.* **1999**, *121*, 3730−3744.
(58) Tao, T. Time-Dependent Fluorescence Depolarization and Brownian Rotational Diffusion Coefficients of Macromolecules. *Biopolymers* **1969**, *8*, 609−632.
(59) Nishida, J.; Fayer, M. D. Theory of Third-Order Spectroscopic Methods to Extract Detailed Molecular Orientational Dynamics for Planar Surfaces and other Uniaxial Systems. *J. Chem. Phys.* **2014**, *140*, 144702.
(60) Gallegos, D. P.; Munn, K.; Smith, D. M.; Stermer, D. L. A NMR Technique for the Analysis of Pore Structure: Application to Materials with Well-Defined Pore Structure. *J. Colloid Interface Sci.* **1987**, *119*, 127−140.
(61) Korb, J. P.; Delville, A.; XU, S.; Demeulenaere, G.; Costa, P.; Jonas, J. Relative Role of Surface Interactions and Topological Effects in Nuclear Magnetic Resonance of Confined Liquids. *J. Chem. Phys.* **1994**, *101*, 7074−7081.
(62) Piletic, I. R.; Moilanen, D. E.; Spry, D. B.; Levinger, N. E.; Fayer, M. D. Testing the Core/Shell Model of Nanoconfined Water in Reverse Micelles Using Linear and Nonlinear IR Spectroscopy. *J. Phys. Chem. A* **2006**, *110*, 4985−4999.

DOI: 10.1021/acs.jpcc.9b00593
J. Phys. Chem. C 2019, 123, 5790−5803

(63) Moilanen, D. E.; Fenn, E. E.; Wong, D. B.; Fayer, M. D. Water Dynamics in Large and Small Reverse Micelles: From Two Ensembles to Collective Behavior. *J. Chem. Phys.* **2009**, *131*, 014704.
(64) Yuan, R.; Yan, C.; Nishida, J.; Fayer, M. D. Dynamics in a Water Interfacial Boundary Layer Investigated with IR Polarization Selective Pump-probe Experiments. *J. Phys. Chem. B* **2017**, *121*, 4530−4537.
(65) Pieniazek, P. A.; Lin, Y.-S.; Chowdhary, J.; Ladanyi, B. M.; Skinner, J. L. Vibrational Spectroscopy and Dynamics of Water Confined inside Reverse Micelles. *J. Phys. Chem. B* **2009**, *113*, 15017−15028.
(66) Asbury, J. B.; Steinel, T.; Stromberg, C.; Corcelli, S. A.; Lawrence, C. P.; Skinner, J. L.; Fayer, M. D. Water Dynamics: Vibrational Echo Correlation Spectroscopy and Comparison to Molecular Dynamics Simulations. *J. Phys. Chem. A* **2004**, *108*, 1107−1119.
(67) Asbury, J. B.; Steinel, T.; Kwak, K.; Corcelli, S. A.; Lawrence, C. P.; Skinner, J. L.; Fayer, M. D. Dynamics of Water Probed with Vibrational Echo Correlation Spectroscopy. *J. Chem. Phys.* **2004**, *121*, 12431−12446.
(68) Corcelli, S. A.; Lawrence, C. P.; Skinner, J. L. Combined Electronic Structure/Molecular Dynamics Approach for Ultrafast Infrared Spectroscopy of Dilute HOD in Liquid H_2O and D_2O. *J. Chem. Phys.* **2004**, *120*, 8107−8117.
(69) Moilanen, D. E.; Fenn, E. E.; Wong, D.; Fayer, M. D. Water Dynamics in Large and Small Reverse Micelles: From Two Ensembles to Collective Behavior. *J. Chem. Phys.* **2009**, *131*, 014704.
(70) Kramer, P. L.; Nishida, J.; Fayer, M. D. Separation of Experimental 2D IR Frequency-Frequency Correlation Functions into Structural and Reorientation-Induced Contributions. *J. Chem. Phys.* **2015**, *143*, 124505.
(71) Kramer, P. L.; Nishida, J.; Giammanco, C. H.; Tamimi, A.; Fayer, M. D. Observation and Theory of Reorientation-Induced Spectral Diffusion in Polarization-Selective 2D IR Spectroscopy. *J. Chem. Phys.* **2015**, *142*, 184505.
(72) Laage, D.; Hynes, J. T. On the Molecular Mechanism of Water Reorientation. *J. Phys. Chem. B* **2008**, *112*, 14230−14242.
(73) Luo, R.-S.; Jonas, J. Raman Scattering Study of Liquid Ethylene Glycol Confined to Nanoporous Silica Glasses. *J. Raman Spectrosc.* **2001**, *32*, 975−978.
(74) Zhang, J.; Jonas, J. NMR Study of the Geometric Confinement Effects on the Anisotropic Rotational Diffusion of Acetonitrile-d3. *J. Phys. Chem.* **1993**, *97*, 8812−8815.
(75) Tros, M.; Zheng, L.; Hunger, J.; Bonn, M.; Bonn, D.; Smits, G. J.; Woutersen, S. Picosecond Orientational Dynamics of Water in Living Cells. *Nat. Commun.* **2017**, *8*, 904.

DOI: 10.1021/acs.jpcc.9b00593
J. Phys. Chem. C 2019, 123, 5790−5803